journal

J. Am. Ceram. Soc., 98 [12] 3948–3955 (2015)
DOI: 10.1111/jace.13848
© 2015 The American Ceramic Society

Nanoscale Microstructural and Chemical Analysis of SiO_2–$Zn_{1-x}Al_xO$ Nanocomposites: Towards a Better Understanding of Si and Al Substitution in ZnO

Matthieu Gilbert,[‡,†] Celine Byl,[§] David Berardan,[§,†] Alexandre Gloter,[¶] Nita Dragoe,[§] and François Vurpillot[‡]

[‡]GPM, UMR CNRS 6634, University of Rouen, Avenue de l'université F-76801, Saint Etienne du Rouvray, France

[§]SP2M, ICMMO, UMR CNRS 8182, University of Paris-Sud, F-91405 Orsay, France

[¶]LPS, UMR CNRS 8502, University of Paris-Sud, F-91405 Orsay, France

In this study, we report on the microstructure of SiO_2-coated Al-doped ZnO nanoparticles densified by spark plasma sintering(SPS), using a multiscale approach. Our observations show that it is possible to successfully prepare dense pellets while keeping the nanostructure with well-defined Si-rich grain boundaries. Although a very limited partial solubility of Si in the ZnO matrix has been observed, Si is mostly concentrated at the grain boundaries. More surprisingly, we evidenced some areas with nanoscale inhomogeneity of the Al concentration, which can locally strongly exceed the average composition of the matrix. It could explain the apparent discrepancy observed in the literature between the simultaneous presence of $ZnAl_2O_4$ in Al-doped ZnO, which should be the signature of the doping level exceeding the solubility limit, and the concentration of carriers that still depends on the nominal Al concentration in ZnO even in the presence of $ZnAl_2O_4$.

I. Introduction

Current annual global energy consumption is about 1.5×10^{14} kWh, and it is estimated to rise by more than 50% before 2040.[1] However, about 65% of the primary energy used in power plants or combustion engines is lost as waste heat. Thermoelectric modules, which can be used to convert heat into electrical power, could play a great role in the energy transition and in the greenhouse gas emissions mitigation through energy efficiency gains.[2] The performance of a thermoelectric material is a growing function of the so-called dimensionless thermoelectric figure of merit ZT, defined as $ZT = (S^2T)/(\rho\lambda)$, where S, ρ, λ, and T are the Seebeck coefficient, the electrical resistivity, the thermal conductivity, and the absolute temperature, respectively. Up to now, the materials available in the middle and high-temperature range are still limited because of the low efficiency/cost ratio and the presence of scarce or toxic elements (lead, tellurium, etc.). Moreover, all materials that exhibit ZT values larger than 1, which constitutes a benchmark for large-scale applications, are intermetallic materials and cannot be use under air because of their poor resistance versus oxidation.[3,4] Consequently, oxide materials have been extensively studied because of their low toxicity, thermal stability, resistance to corrosion at high temperatures and low-cost, although to date their performances are lower than those of intermetallic systems.[5,6]

Zinc-oxide-based materials are among the best n-type thermoelectric oxides, with ZT values as high as 0.65 at 1000°C, although some of the results previously reported regarding these performances are controversial.[7–9] ZnO is a wide band gap semiconductor (E_g = 3.4 eV), which exhibits reasonably large electron mobility.[10] When appropriately doped, mostly by substituting 3+ or 4+ cations on the Zn^{2+} site, the electron concentration increases leading to electrical resistivity values of the order of 1 mΩ·cm.[7] As a consequence, the thermoelectric power factor, defined as $PF = S^2/\rho$, exceeds 1 mW m^{-1} K^{-2}, which is of the order of magnitude of the state-of-the-art intermetallic materials.[7] However, due to the very simple würtzite crystal structure and the presence of light elements, the thermal conductivity is much larger than that of conventional thermoelectric materials, which is detrimental for the thermoelectric figure of merit.[8] Therefore, the best ZT values are obtained in "over-doped" $Zn_{1-x}Al_xO$, where Al synergistically acts as a dopant and as the precursor of a $ZnAl_2O_4$ spinel phase dispersed in the matrix, which contributes to a grain size reduction by the pinning of the grain boundaries and to phonons scattering.[11] The same results has been obtained with multinary-doped $Zn_{1-x-y}Al_xM_yO$ with Al^{3+} exceeding the solubility limit,[7] which has been reported as 0.3% by secondary ion mass spectroscopy (SIMS) analysis,[12,13] and M being another doping element. The strategy of using a nanocrystalline secondary phase dispersed in a thermoelectric matrix to decrease the thermal conductivity has been widely used in the thermoelectric community with a good success.[4] However, in the particular case of $Zn_{1-x}Al_xO$, the secondary phase only appears when Al^{3+} concentration exceeds the solubility limit, which precludes the simultaneous control of both the electron concentration, through the doping level, and of the spinel phase fraction and dispersion. Moreover, although this material has been thoroughly studied, the doping mechanisms in $Zn_{1-x}Al_xO$ remain unclear to date, as the electron concentration still depends on the nominal Al fraction even above the solubility limit, at least in certain synthesis conditions.[9,14,15] A solution to uncouple the control of the doping level and the control of the secondary phase dispersion would be to choose another secondary phase, without zinc and aluminum, and which would be chemically stable in the $Zn_{1-x}Al_xO$ matrix or at least exhibit a negligible solubility. In addition, if dispersed at the grain boundaries, this secondary phase could act as a filter for the carriers and could lead to an enhancement of the thermoelectric power factor.[16] SiO_2 is known to strongly reduce the grain growth during ZnO sintering.[17] Moreover, SiO_2-coated ZnO nanoparticles can be easily

J. Ihlefeld—contributing editor

Manuscript No. 36729. Received May 13, 2015; approved July 21, 2015.
[†]Authors to whom correspondence should be addressed. e-mails: matthieu.gilbert@univ-rouen.fr and david.berardan@u-psud.fr

obtained using chemical synthesis routes.[18–20] Last, it is not very clear whether Si can act as an active dopant in ZnO or not. Indeed, a significant enhancement of the concentration of carriers has already been reported in thin-film of Si-doped ZnO,[21] but never in bulk materials. Therefore, we have synthesized $Zn_{1-x}Al_xO$ nanoparticles (with Al concentration $x = 0.002$, slightly lower than the solubility limit), which have been subsequently coated by SiO_2 and densified, to obtain dense $Zn_{1-x}Al_xO$-SiO_2 nanocomposites with simultaneous control of the doping level and of the nanocrystalline secondary phase dispersion. In this study, we report on the nano/microstructure of the obtained composites and on the dispersion of the elements in the matrix.

II. Experimental Details

Al-doped ZnO nanoparticles with nominal composition $Zn_{0.998}Al_{0.002}O$ were synthesized using a modified polyol method. Benzoïc acid (99%; Alfa Aesar, Ward Hill, MA) was used as surfactant to limit the growth of the nanoparticles during the synthesis process. Zinc acetate dihydrate (99.997%; Sigma-Aldrich, St Louis, MO), aluminum nitrate nonahydrate (99.997%; Sigma-Aldrich) benzoïc acid (BA/Zn = 0.2), distilled water ($n_{H2O}/n_{Zn} = 4$), and ethylene glycol (99%, 80 mL; Alfa Aesar) were put into a 100 mL flask fitted with a reflux condenser. The solution was stirred vigorously, heated to a temperature of 160°C, kept 1 h at this temperature, and cooled naturally to room temperature. The particles were separated by centrifugation and washed with ethanol and then with water. Then, they were dried by lyophilization after dispersion in water. Last, they were calcinated at 410°C during 30 min under flowing O_2 with a heating rate of 0.5 K/min.

The nanoparticles were coated by SiO_2 using atomic layer deposition in a glass tube, following the method developed by Hatton et al.,[18] as shortly described below.

The silica growth was performed using two 380 mL glass tubes (2.5 cm diameter) containing 10 mL of tetramethyl orthosilicate (TMOS; 98%; Sigma-Aldrich) and 10 mL ammonium hydroxide (30 wt% solution; Sigma-Aldrich). 300 mg of ZnO nanoparticles were put into a glass crucible, whose bottom is a filter disk with glass rim of porosity 1. The powder was exposed alternately in each tube, approximately 2 cm above the liquid surface, for 1 min in the TMOS atmosphere and 10 min in NH_3/H_2O vapors. This cycle was repeated 10 times. The modified powder was dried one night at 80°C under air.

ZnO powder and modified ZnO were sintered using a Syntec-SPS-511S spark plasma sintering (SPS) system at 850°C with 5 min holding time in a $\Phi = 10$ mm graphite mold under an axial compressive stress of 120 MPa, under dynamic primary vacuum. A heating rate of 100°C/min was used. The increase in pressure was performed with a rate of 15 MPa/min. After the densification process, the samples were annealed under flowing oxygen at 600°C for 24 h to release possible strains and eliminate possible oxygen vacancies that could be due to the sintering method.

Specific surface area was measured by the Brunauer–Emmett–Teller (BET) method on a BELSORP II (BEL, Osaka, Japan) gas sorption analyzer by nitrogen sorption on samples that were previously degassed 2 h at 120°C.

X-Ray diffraction characterization was performed using a Panalytical X'Pert diffractometer (PANanlytical, Almeno, the Netherlands) using a Cu$K_{\alpha 1}$ radiation obtained using a Ge (111) incident monochromator and an X'celerator detector. Rietveld refinements were performed using FULLPROF software.[22]

Room-temperature optical diffuse reflectance measurements were performed on finely ground powders. The spectra were collected in a Varian Cary 5000 double-beam, double-monochromator spectrophotometer, with a PTFE integrating sphere (Varian, Palo Alto, CA).

The microstructure of the densified samples was observed on fractured surfaces using a field-emission gun scanning electron microscope (SIGMA ZEISS, Oberkochen, Germany). Energy dispersive mapping analysis using EDX (EDAX-TSL) was carried out to evaluate the distribution of the elements in the samples. The morphology of the nanoparticles was investigated using a JEOL JEM 2011 transmission electron microscope (TEM) (JEOL Ltd., Tokyo, Japan). To study the crystallinity and chemical distribution of Si in the coated samples, a thin section was prepared by focus ion beam. STEM and EELS experiments have been performed using a NION USTEM microscope operating at 200 kV (Nion, Kirkland, WA).

To perform atom probe experiments, the samples have to be prepared in the form of a sharp tip with an end radius in the range of tens of nanometer. Indeed, atoms from the surface of the sample are then ionized by a strong electric field generated by the application of a kilovolts-range potential.[23–25] Apart from metals, this particular shape is obtained using a dual beam SEM FIB to annular mill the sample. Ion milling can only be done on small pieces of material (typical size 5 μm × 5 μm × 10 μm). Usually, this size is reached by milling the substrate and lifting out the lamella.[26,27] Nevertheless, this method is time-consuming and is particularly well-adapted for planar substrate and for structures that have to be precisely located in space. In our case, the sample can be seen as a bulk material. The pellet obtained after SPS is macroscopically homogeneous in volume and therefore there is no requirement for precise location for the tip preparation. For this reason, the sharp shards method proposed by Melmed has been used.[28] With the help of an optical microscope equipped with a micromanipulator, sharp shards with the good size and shape have been glued (using conductive silver epoxy) on a tungsten needle and then annular milled.

III. Results and Discussion

Following the synthesis route described in the experimental section, a well-dispersed white powder has been obtained, with a large BET-specific surface area of 67 m^2/g. Assuming spherical particles and no agglomeration, it corresponds to a particle radius of 15 nm. This radius is fully consistent with the TEM observations (see later), which confirms that the particles are not agglomerated. Figure 1 shows the XRD pattern before coating. All peaks can be indexed in the ZnO-type structure, and no secondary phase can be observed. This result was expected as the nominal Al concentration is smaller than the reported solubility limit. However, the Bragg peaks are broad, due to the nanocrystalline character of the sample, and we cannot exclude at this stage the presence of small amounts of nanocrystalline secondary phases. As it can be observed in Fig. 1, there is no evolution of the XRD pattern during the coating process. The lattice parameters obtained using Rietveld refinement are the same for the coated and as-synthesized particles, within the error bar (lattice parameters cannot be determined very precisely for nanocrystalline particles). Therefore, we cannot confidently conclude at this stage that a chemical reaction occurred during the coating process.

The widening of the Bragg peaks observed in the diffraction patterns is consistent with the TEM observations, presented in Fig. 2. Before coating (left), the size of the particles is about 14 nm, and crystalline planes are clearly visible. Moreover, the surface of the particles has well-defined low index planes (see inset), and shows no amorphous phase, as, for example, aluminum or zinc hydroxide. After coating (right), a clear evolution of the surface of the particles can be observed. It exhibits a clear roughness, and some disorder characteristic of an amorphous layer can be observed on some particles. Although it is not possible to measure the thickness of this faint amorphous layer, it confirms that the surface of the particles has changed during the coating pro-

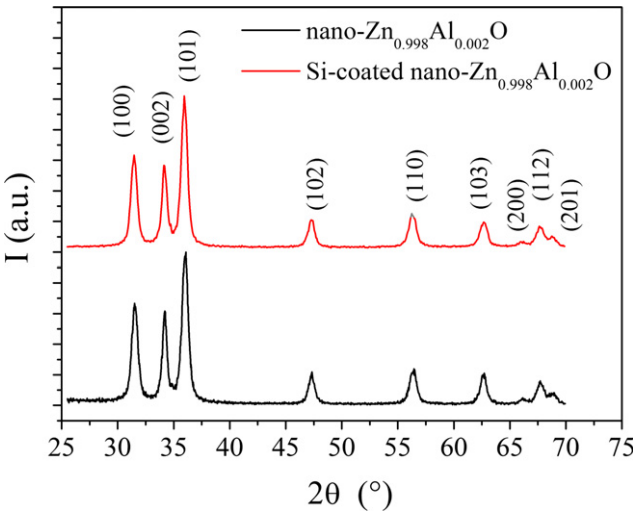

Fig. 1. XRD patterns of the as-synthesized ZnO nanoparticles and the coated nanoparticles.

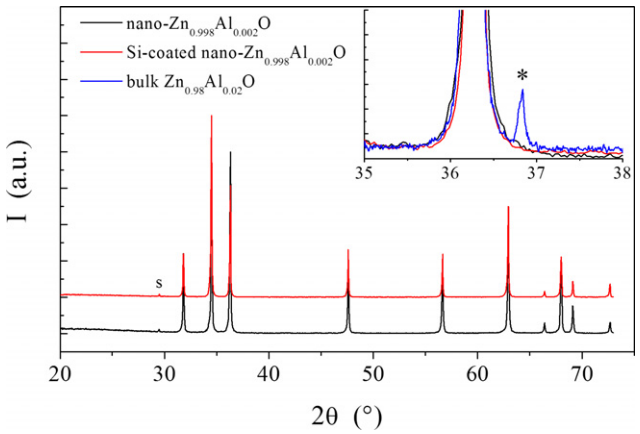

Fig. 3. XRD patterns of nano-$Zn_{0.998}Al_{0.002}O$ and coated nano-$Zn_{0.998}Al_{0.002}O$ after SPS. The peak marked with the "s" is due to the sample holder. The inset shows the same diffraction patterns in the 35°–38° angular range, as compared to the diffraction pattern of bulk $Zn_{0.98}Al_{0.02}O$ (from Ref. [9]). The peak marked with a "*" corresponds to the $ZnAl_2O_4$ spinel phase.

cess. To confirm the chemical nature of the amorphous layer, we have performed ICP measurements of the composition of the as-synthesized particles and of the coated particles. Before coating, the cationic composition of the particles mostly consists in Zn and faint amount of Al. After coating, Si can also be detected, which confirms that the amorphous layer most probably contains amorphous silica.

The SPS process lead to well-densified pellets, with geometrical density of about 96% of the theoretical density. Figure 3 shows the XRD patterns after SPS densification. All the peaks can be indexed in the ZnO-type structure for both samples. More especially, no $ZnAl_2O_4$ spinel can be detected, as it can be observed in the inset that compares the XRD patterns of the coated and uncoated nano-$Zn_{0.998}Al_{0.002}O$ samples to that of bulk $Zn_{0.98}Al_{0.02}O$, whose diffraction pattern evidenced the presence of the spinel phase.[9] Moreover, no difference can be observed between the diffraction patterns of the coated and uncoated samples, which is further confirmed by the lattice parameters obtained by Rietveld refinement, which are the same for both samples. Therefore, it seems that either there is no Zn substitution by Si, or if substitution occurs the solubility limit is very low and does not induce a noticeable change in the lattice parameters despite the large difference between the ionic radii of Zn^{2+} and Si^{4+}.[29]

Figure 4 shows the SEM images of fractured pellets. Without coating, a very significant grain growth occurred during the densification process, with mean grain size of about 550 nm. The coated sample also experienced a significant grain growth. However, it can be clearly observed that the mean grain size is significantly smaller than the one of the uncoated sample, and is close to 180 nm, which confirms that the coating layer was effective in pinning the grain boundaries and limiting the grain growth during the densification process, similar to the situation observed in $ZnAl_2O_4$-containing samples,[9,11] while keeping a good densification with no significant increase of the porosity of the pellet. No secondary phase can be observed in the SEM picture. This result confirms that the aluminum fraction chosen for this study is smaller than the solubility limit, which prevents the formation of the spinel secondary phase. Moreover, it suggests that no silicate phase formed during the synthesis and densification processes of the coated particles and that no silica segregation occurred. However, this latest observation might seem surprising. Indeed, as the starting powder consisted in nano-$Zn_{0.998}Al_{0.002}O$ particles coated with silica (or a Si-containing amorphous layer), the presence of silica or silicates nanoparticles at the grain boundaries was expected after the SPS process. The absence of such nanoparticles could possibly be explained by a solubility of Si in ZnO, although no change in the lattice parameters was observed. As mentioned in the introduction, it is not clear whether Si can substitute Zn in the ZnO matrix or not. Effective Si doping has already been mentioned in $Zn_{1-x}Si_xO$ thin films,[21] but never in bulk materials. Figure 4 also shows EDX mapping in the case of the Si-coated sample. The size of the analyzed area, 3 μm x 3 μm, is much larger than the grain size, which ensures that many grain boundaries are present. The black spots in Fig. 4(a), which is the SEM picture of the area

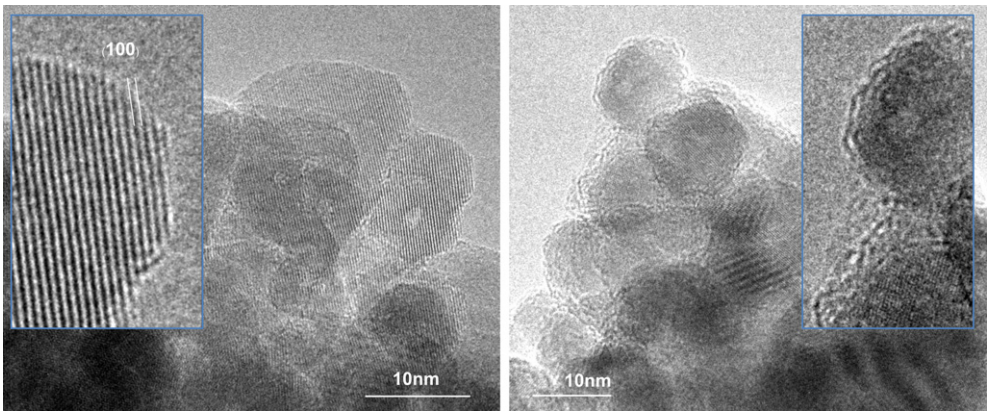

Fig. 2. TEM observations of the as-synthesized ZnO nanoparticles (left) and the coated nanoparticles (right).

analyzed in Fig. 4(b), correspond to holes in the surface of the sample occurring during the polishing step. A perfectly homogeneous distribution of Zn and Al atoms has been observed (not shown), which confirms that no $ZnAl_2O_4$ particles formed during the synthesis, or that they are smaller than the spatial resolution of the EDX mapping. Regarding the Si distribution [Fig. 4(b)], it is relatively homogeneous, although a slight contrast can be noticed in the picture corresponding to Si-enriched areas. However, as these Si-enriched areas do not correlated with Zn or Al depletion, it is not possible to conclude about their nature confidently.

Following this observation, UV–Vis spectroscopy has been performed to detect a possible doping effect of Si, as a change in the concentration of carriers should lead to an evolution of the optical band gap due to Burstein-Moss effect. The diffused reflectance spectra observed at room temperature were converted using Kubelka–Munk relation:

$$\frac{A}{S} = \frac{(1-R)^2}{2R}$$

with R the absolute reflectance of the sample, A the molar absorption coefficient, and S the scattering coefficient. A clear band edge structure can be observed in Fig. 5, which indicates that the band gap is in the near-UV region for all samples. The band edge structure of the nanocrystalline coated and uncoated $Zn_{0.998}Al_{0.002}O$ samples before SPS densification are very similar, without any noticeable shift of the band gap within the precision of the measurement method.

At this stage, it would be interesting to estimate the concentration of electroactive species that could be detected through an evolution of the band-gap. At low doping levels, the electronic band structure of ZnO is well described in a single-parabolic band model. Therefore, we can neglect the possible change in the effective mass of the carriers with their concentration, in a first approximation. Two mechanisms can induce a shift of the band gap. On the one side, the Burstein–Moss shift corresponds to a slight widening of the *optical* band gap due to the increased concentration of carriers. This shift is partly counterbalanced by a possible slight narrowing of the *electrical* band gap originating from electron–electron and electron-ionized impurities interactions. This second effect is generally smaller than the Burstein–Moss shift, and can probably be neglected in a first approximation if the Si concentration within the ZnO particles is

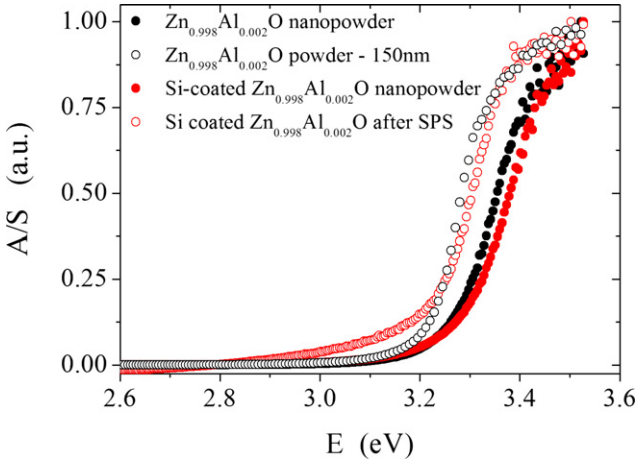

Fig. 5. UV–Vis spectroscopy (for the definition of the y-axis, see text) obtained from reflexion spectra of $Zn_{0.998}Al_{0.002}O$ as-synthesized nanoparticles (diameter 14 nm), Si-coated $Zn_{0.998}Al_{0.002}O$ nanoparticles, Si-coated nano-$Zn_{0.998}Al_{0.002}O$ after densification by SPS, and $Zn_{0.998}Al_{0.002}O$ with controlled grain growth (see text, diameter 150 nm).

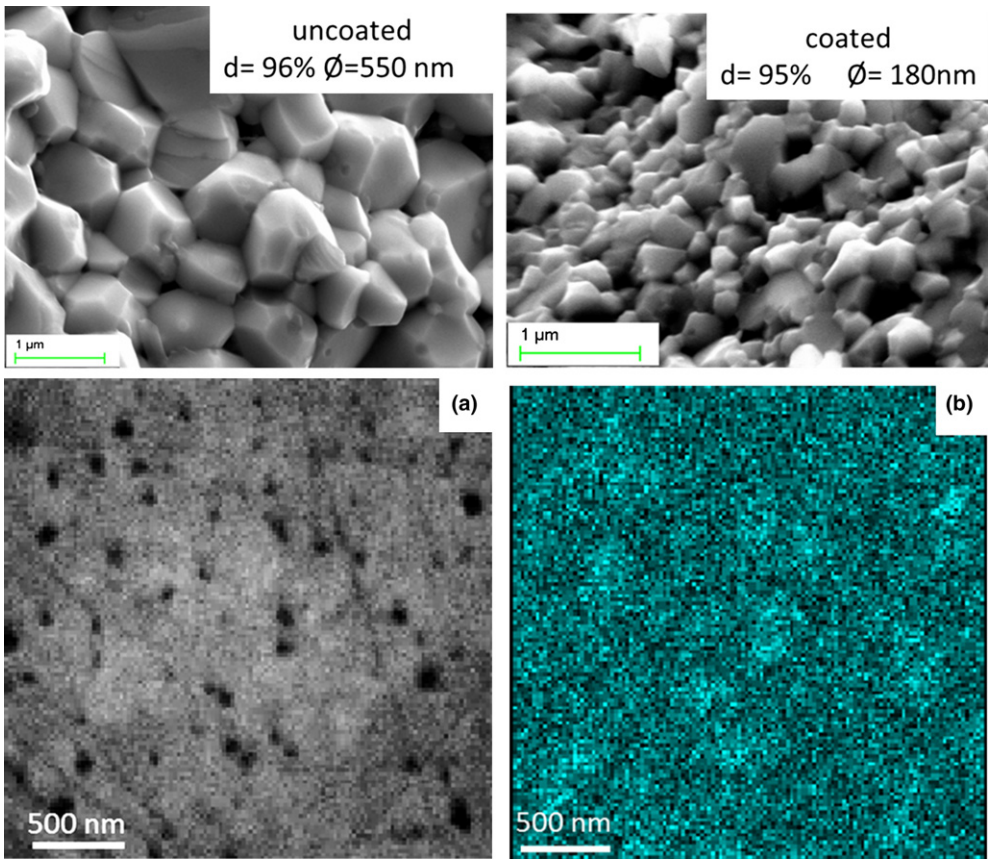

Fig. 4. SEM image of uncoated $Zn_{0.998}Al_{0.002}O$ nanoparticles and Si- coated $Zn_{0.998}Al_{0.002}O$ after densification by SPS. SEM image (a) of the polished area corresponding to the EDS analysis. Distribution of Si (b) in Si-coated nano-$Zn_{0.998}Al_{0.002}O$ obtained by EDS analysis.

small. Regarding the Burstein–Moss shift, it is given by the following relation, in a single-parabolic band model:

$$\Delta E_{\mathrm{BM}} = \frac{\hbar^2}{2m^*_{\mathrm{he}}}(3\pi^2 n)^{2/3}$$

with ΔE_{BM} the shift of the band gap due to Burstein–Moss effect, n the difference between the concentration of carriers of the two samples, and m^*_{he} the reduced effective mass. In ZnO, m^*_{he} can be estimated of the order of $0.19m_{\mathrm{e}}$ with m_{e} the electron rest mass.[10]

With a detection limit of the band gap shift of 0.05 eV, a difference of concentration of carriers of 5×10^{18} cm^{-3} could be detected under these approximations. This value would correspond to 1×10^{-4} electron per formula unit. Therefore, the absence of any noticeable difference between Si-coated and uncoated $Zn_{0.998}Al_{0.002}O$ nanoparticles means either that there is no substitution of Zn by Si (or a very limited one) during the coating process and particles annealing, or that Si is not electroactive in ZnO.

After SPS, a clear redshift of the optical band gap can be observed, which can be explained by the increase in the grain size during the densification process. However, the optical band gap of Si-coated and uncoated $Zn_{0.998}Al_{0.002}O$ cannot be directly compared after SPS. Indeed, the grain size in these samples is significantly different, with a blueshift for smaller grain size.[30,31] Therefore, we have performed an annealing treatment of the uncoated $Zn_{0.998}Al_{0.002}O$ nanoparticles with a controlled grain growth to obtain a similar mean grain size as in Si-coated $Zn_{0.998}Al_{0.002}O$ after SPS. After this controlled annealing that lead to 150 nm particles, a clear redshift of the optical band gap can be observed, consistent with the grain growth.[30,31] Interestingly, this redshift is the same as the one experienced by the Si-coated sample after SPS, and no significant difference can be seen between the optical band gap of the Si-coated nano-$Zn_{0.998}Al_{0.002}O$ after densification by SPS and the $Zn_{0.998}Al_{0.002}O$ powder with controlled grain growth within the precision of the measurement method (although the band edge is not so well-defined for the former one). Therefore, either there is no substitution of Zn by Si in the ZnO matrix during the SPS and postannealing processes (or a very small one), or Si is not electroactive in ZnO or exhibit a poor doping efficiency. This result strongly contrasts with the results obtained in Si-doped ZnO thin films, where a significant blueshift of the optical band gap has been observed upon doping due to the increased concentration of carriers.[21] Therefore, we have investigated the localization of Si atoms in the sample at the nanoscale.

Figures 6(a) shows the TEM bright-field (BF) image, which shows grains with typical size of 150 nm and different crystallographic orientations. Figure 6(b) shows the STEM-BF image of a grain boundary (GB) measured at higher magnification. It reveals a very high crystalline order of both grains limiting the spatial extension of the boundaries core below one nanometer. The STEM-HAADF image in Fig 6(c) shows a triangular low-density area in between grain typical of a triple pocket. To investigate the chemical composition of these grain boundaries, electron energy loss spectroscopy (EELS) has been carried out using an angstrom size probe. Profile 6(d) describes GB core <1 nm. The Si/Zn ratio estimated for the spectrum extracted from the core of the GB (half-width <0.3 nm) is estimated to about 0.4, which evidences a strong silicon enrichment at the atomic planes composing the GB. At several nanometers away from the GB core, the EELS silicon signal is already undetectable [Fig. 6(e)]. Based on computed cross section and estimated signal to noise ratio, this indicates that the residual amount of silicon away from the GB is below 1%, otherwise it would have been detected in the EELS spectra. These observations shows that it is possible to prepare dense pellets with grain boundaries that simultaneously exhibit a very good crystalline order, favorable for intergrain electrical transport, and composition modification at the nanoscale, which can induce a controlled potential barrier for the conduction of carriers

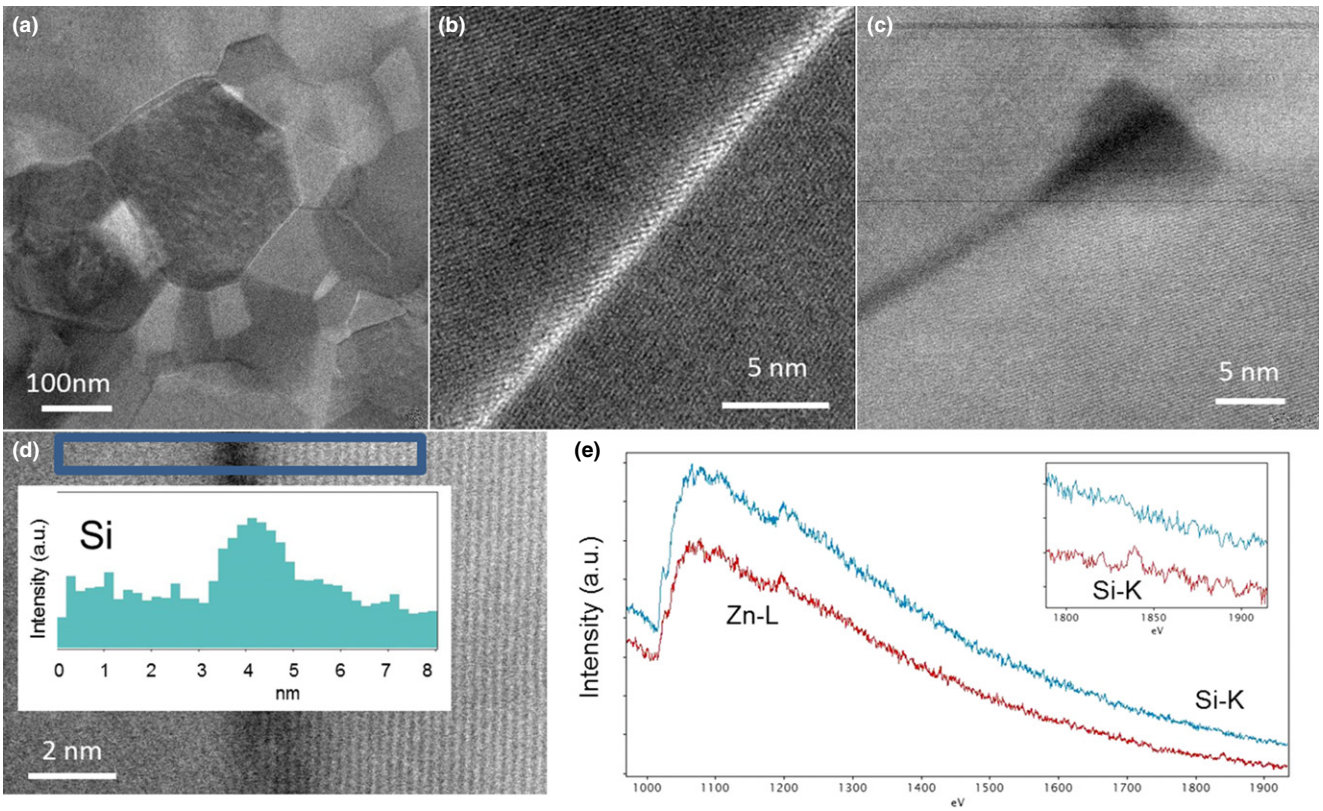

Fig. 6. (a) STEM-BF showing submicrometer size grains; (b) STEM-BF image of a grain boundary, (c) nanoscale inclusion, (d,e) EELS analysis of a grain boundary.

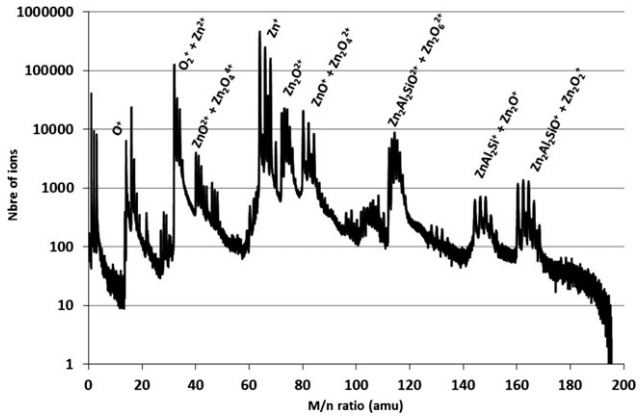

Fig. 7. Total mass spectrum obtained from the analysis of SiO_2-coated Al-doped ZnO sintered nanoparticles.

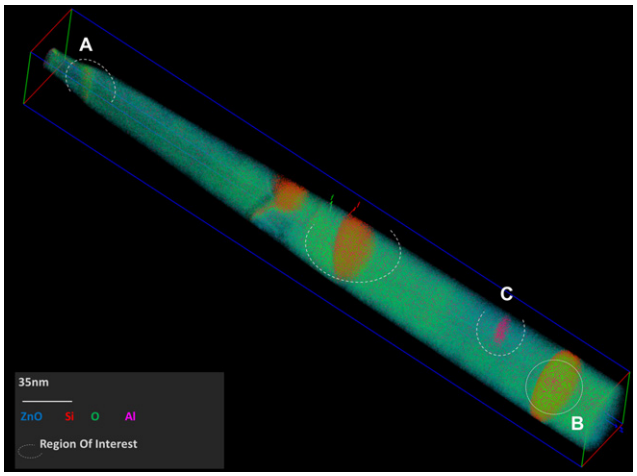

Fig. 8. 3D reconstruction of the analyzed volume. The volume exhibits a complex nanostructure with many ZnO grains (grain boundaries seems to be Si and O enriched), Si-enriched particles (B) and Al cluster (C).

as well as strong phonons scattering. Due to similar statistical issue, the EELS signal of the Al–K, with nominal concentration as low as 0.2%, has never been detected. At the triple pocket, the EELS signal of silicon can easily be detected. This might indicate the presence of a silicon-enriched oxide film surrounding the grains. We have also observed some area appearing as darker in STEM-HAADF and extending over 20–40 nm. The EELS analysis of these area indicate typical Si/Zn ratio ranging from 0.1 to 0.2. The presence of these nanoscale inclusions is consistent with the atom probe observations, see below.

Atom probe measurements of oxide materials became possible with the emergence of laser-assisted field evaporation,[32] but remain difficult because mass spectra exhibit molecular ions and mass overlap. This drawback leads to the need of a careful study of the mass spectra to precisely allocate the correct chemical nature to the peaks. Indeed, precise knowledge of this chemical nature is a key point for both 3D reconstruction and composition measurements. During an atom probe measurement, atoms from the surface of the tip are ionized and collected by a position sensitive detector. Thanks to the known quasistereographic projection law the initial coordinates of the atoms are computed to form a virtual 3D volume.[33] This algorithm simply assumes that the analyzed volume is nothing else than the number of collected ions weighted by the detection efficiency (~75%). Counting the exact number of collected atoms is thus of great importance. In addition, the composition of the studied areas is calculated from the number of collected atoms. With molecular ions, a

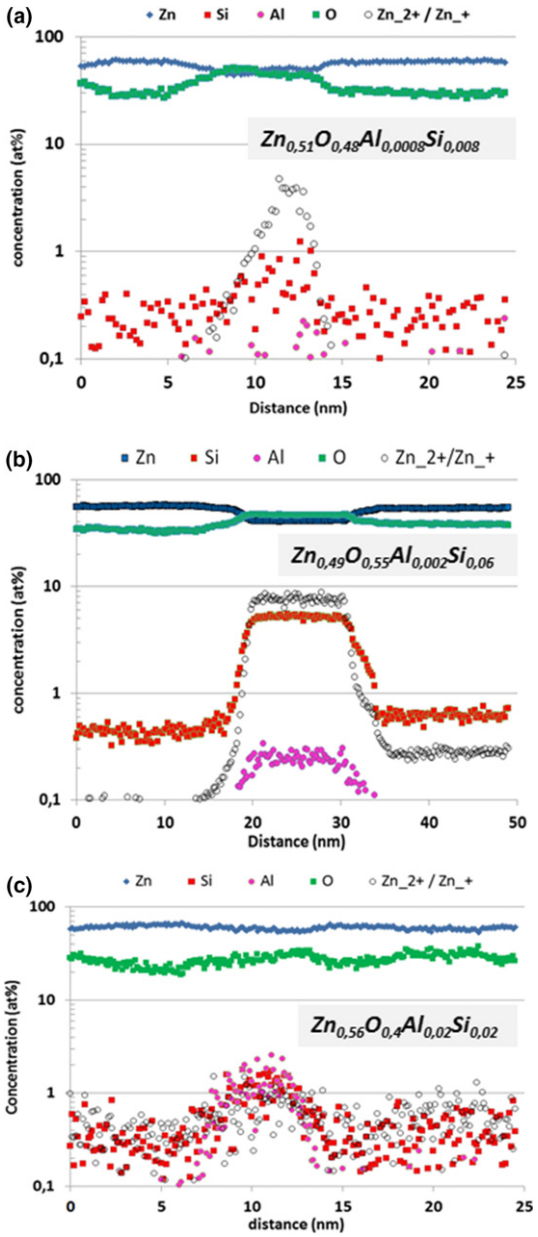

Fig. 9. Depth profiles across the different regions of interest. (a) is the depth profile corresponding to the grain boundary labeled (a) on the analyzed volume (Fig. 12), (b) is the depth profile of the Si-enriched area and (c) the depth profile of the Al-rich area.

count is not an atom but a cluster. The total number of collected atoms is thus clearly different from the number of recorded counts. Accurate composition measurement requires thus a good evaluation of the effective number of collected atoms by an accurate identification of the peaks in the mass spectra. In the case of the Si-coated sample, a lot of molecular ions have been observed, see Fig. 7, which illustrates the need of taking into account mass overlaps and molecular ions to interpret and identify mass peaks with a better accuracy.

Once the elements from the sample have been identified in the mass spectrum, the analyzed volume can be 3D computed (Fig. 8). This picture shows that the nanostructure of the sample is more complex than it could have been expected. Indeed, many ZnO nanograins have been analyzed allowing us to measure the composition of the grain boundaries, which seems to be silicon and oxygen enriched (labeled A in the picture), in agreement with the EELS analysis presented above. Moreover, other areas with different compositions are clearly visible. One seems to be enriched in silicon (labeled B) and another in aluminum (labeled C). The composition of those objects has been

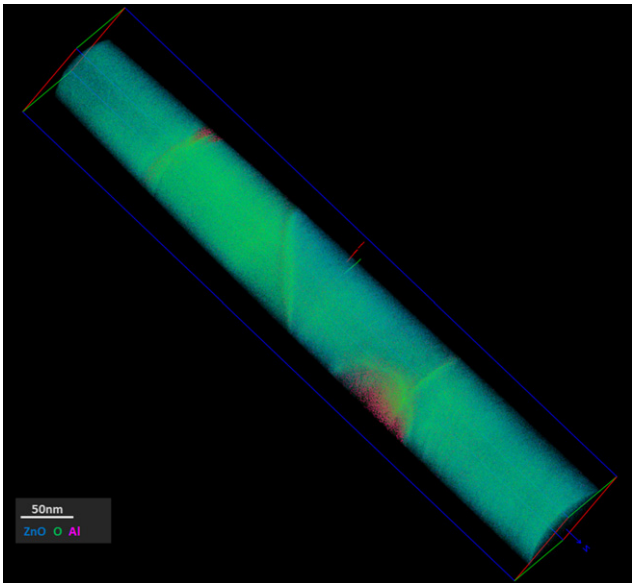

Fig. 10. 3D reconstruction of the analyzed volume of the densified nano-$Zn_{0.998}Al_{0.002}O$ sample without coating.

investigated using depth profiles. Figure 9 summarizes the depth profiles corresponding to the different objects. The profiles confirm the enrichment in Si and O at the grain boundaries, where the estimated concentration of silicon rises up to approximately 1%, whereas it is half in the ZnO grains, whereas no noticeable change in the aluminum concentration occurs. Although the estimation of the compositions is semi-quantitative only, due to the faint amount of Si and Al in the samples, it confirmed the Si enrichment of the grain boundaries as compared to the matrix, as observed by EELS (Fig. 6). In addition, the state of charge ratio Zn^{2+}/Zn^{+} has been also plotted on the composition profile. In atom probe analysis, the state of charge ratio is a good indicator of the magnitude of the electric field at the surface of the sample,[34] which depends on the local chemistry and topography. The increase in the Zn^{2+}/Zn^{+} ratio at the grain boundary indicates that the electric field is larger, which is consistent with a local enrichment in Si and O (SiO is known to have a larger field evaporation than ZnO). This behavior is also observed in the depth profile across the Si–O enriched area (profile b in Fig. 9 and label B in Fig. 8) where Si and O contents increase. However, although a Si enrichment can be locally observed in the object B in Fig. 8, it should be noted that the main constituents of this object remain Zn and O. Therefore, this object does not seem to correspond to a silicate phase or to a Zn-Si mixed oxide, but to Si-enriched ZnO.

Last, the depth profile across the Al-rich area (object C in Fig. 8) shows that the concentration of Al rises up to 2%. The Al concentration in that particle is thus ten times larger than the nominal concentration (0.2%), with a significant increase that can be observed in the profile over a 10 nm width. Similar to the Si-enriched areas, the main constituents remain Zn and O, and this object corresponds to a local Al enrichment of the ZnO phase. This observation is surprising, as the nominal Al concentration in the sample was chosen slightly below the solubility limit estimated in the literature,[12,13] which means that the Al concentration in object C could locally exceed the solubility limit. As profile C also evidenced a moderate increase in the Si concentration in object C, a cooperative mechanism leading to simultaneous Si + Al enrichment of the ZnO matrix may be possible. Therefore, we have also studied the aluminum distribution of a densified nano-$Zn_{0.998}Al_{0.002}O$ sample without Si coating using atom probe analysis. The 3D reconstruction of the analyzed volume (Fig. 10) shows that similar Al-enriched areas are present even in the absence of Si in the sample, which rules out the possibility of a cooperative mechanism. At a first glance, this observation seems contradictory with the literature results regarding the solubility limit of Al in ZnO.[12,13] One possible explanation of this discrepancy could be the different volume scales of the analysis. The resolution of the SIMS analysis used in the literature to estimate the solubility limit of Al in ZnO is of the order of 100 nm × 100 nm, a size corresponding to the entire 3D reconstructed volume in atom probe analysis (Figs. 8 and 10). Moreover, the width of the Al-enriched area in the depth profile is of the order of 10 nm, one order of magnitude smaller than the resolution of the SIMS analysis. Due to this very small size, such local Al enrichment could not have been observed by SIMS analysis, which can only give an averaged composition. However, $ZnAl_2O_4$ spinel phase can be unambiguously observed in Al-doped ZnO samples with nominal Al fraction as low as 0.5%,[9] which might also seem contradictory with our atom probe analysis that shows an Al concentration larger than the supposed solubility limit in the Al-enriched areas. However, this apparent discrepancy could easily be explained by Al concentration in bulk Al-doped ZnO locally exceeding the actual solubility limit and leading to the formation of stable $ZnAl_2O_4$ (Al doping of the ZnO matrix is often performed by the solid-state reaction of ZnO and Al_2O_3), or by fluctuations of the local conditions during the synthesis (temperature, oxygen partial pressure) that could locally influence the equilibrium between Al dissolution in ZnO matrix and $ZnAl_2O_4$ formation, or both mechanism simultaneously. Moreover, it could also explain why the electron concentration of Al-doped ZnO still changes when increasing the nominal Al concentration even when $ZnAl_2O_4$ phase is present (at least for certain synthesis conditions[9,14,15]), which is a signature of a change in the donor Al concentration.

V. Conclusion

To conclude, we have successfully synthesized coated Al-doped ZnO nanoparticles, with a coating layer containing Si. These nanoparticles have been densified by SPS reaching 96% density while keeping the nanoscale microstructure. The absence of $ZnAl_2O_4$ spinel phase, often observed in Al-doped ZnO samples, has been confirmed by XRD, SEM, and USTEM, whereas a Si enrichment of the grain boundaries is maintained after the densification. The presence of Si at the grain boundaries has been further confirmed by atom probe analysis. However, a partial diffusion of Si in the particles has also been noticed. Although Si does not seem electroactive, from the absence of noticeable Burstein–Moss shift in the UV–Vis observations, electrical transport studies should be performed to confirm that "Si coating" of Al-doped ZnO could be used to produce energy filtering of the charge carriers without changing their concentration significantly. In addition, the atom probe analysis has shown that even with a nominal Al concentration below the solubility limit estimated in the literature, Al-enriched areas are present in the ZnO matrix at the nanoscale. This observation shows that the formation of $ZnAl_2O_4$ in Al-doped ZnO, which can be observed for nominal Al concentration as low as 0.5%, may be more complex that simply Al exceeding the solubility limit. This more complex mechanism would be in agreement with the surprising Al concentration dependence of the concentration of carriers of Al-doped ZnO samples containing $ZnAl_2O_4$, widely observed in the literature, and should be further studied.

Acknowledgments

The authors acknowledge support from the ANR through the project Nanoxydesign ANR 2010-BLAN-0814-02. The authors want to thank P. Ribot for SEM observations and EDX characterization.

References

[1]International Energy Outlook 2010. U.S. Energy Information Administration, U.S. Department of Energy, 1–8, 2010.

[2]J.-P. Fleurial, "Thermoelectric Power Generation Materials: Technology and Application Opportunities," *JOM*, **61**, 79–85 (2009).

[3]J. R. Sootsman, D.-Y. Chung, and M. G. Kanatzidis, "New and Old Concepts in Thermoelectric Materials," *Angew. Chem. Int. Ed.*, **48**, 8616–39 (2009).

[4]S. K. Bux, J.-P. Fleurial, and R. B. Kaner, "Nanostructured Materials for Thermoelectric Applications," *Chem. Comm*, **46**, 8311–24 (2010).

[5]J. He, Y. Liu, and R. Funahashi, "Oxide Thermoelectrics: The Challenges, Progress, and Outlook," *J. Mater. Res.*, **26**, 1762–72 (2011).

[6]K. Koumoto, et al., "Thermoelectric Ceramics for Energy Harvesting," *J. Am. Ceram. Soc.*, **96**, 1–23 (2012).

[7]M. Ohtaki, K. Araki, and K. Yamamoto, "High Thermoelectric Performance of Dually Doped ZnO Ceramics," *J. Electron. Mater.*, **38**, 1234–8 (2009).

[8]M. Ohtaki, T. Tsubota, K. Eguchi, and H. Arai, "High-Temperature Thermoelectric Properties of $Zn_{1-x}Al_xO$," *J. Appl. Phys.*, **79**, 1816–8 (1996).

[9]D. Bérardan, C. Byl, and N. Dragoe, "Influence of the Preparation Conditions on the Thermoelectric Properties of Al-Doped ZnO," *J. Am. Ceram. Soc.*, **93**, 2352–8 (2010).

[10]H. Morkoc and U. Ozgur, *Zinc Oxide: Fundamentals, Materials and Device Technology*. WILEY-VCH Verlag GmbH, Weinheim, Germany, 2009.

[11]N. Ma, J.-F. Li, B. P. Zhang, Y.-H. Lin, L. R. Ren, and G. F. Chen, "Microstructure and Thermoelectric Properties of $Zn_{1-x}Al_xO$ Ceramics Fabricated by Spark Plasma Sintering," *J. Phys. Chem. Sol.*, **71**, 1344–9 (2010).

[12]K. Shirouzu, T. Kawamoto, N. Enomoto, and J. Hojo, "Dissolution Behavior of Al and Formation Process of $ZnAl_2O_4$ Phases in Al_2O_3-Doped ZnO Sintered Bodies," *Jpn. J. Appl. Phys.*, **49**, 010201, 3pp (2010).

[13]K. Shirouzu, T. Ohkusa, M. Hotta, N. Enomoto, and J. Hojo, "Distribution and Solubility Limit of Al in Al_2O_3-Doped ZnO Sintered Body," *J. Ceram. Soc. Jpn.*, **115**, 254–8 (2007).

[14]E. Guilmeau, A. Maignan, and C. Martin, "Thermoelectric Oxides: Effect of Doping in Delafossites and Zinc Oxide," *J. Electron. Mater.*, **38**, 1104–8 (2009).

[15]J. P. Wiff, Y. Kinemuchi, H. Kaga, C. Ito, and K. Watari, "Correlations Between Thermoelectric Properties and Effective Mass Caused by Lattice Distorsion in Al-Doped ZnO Ceramics," *J. Eur. Ceram. Soc.*, **29**, 1413–18 (2009).

[16]D. L. Medlin and G. J. Snyder, "Interfaces in Bulk Thermoelectric Materials," *Curr. Opin. Colloid Interface Sci.*, **14**, 226–35 (2009).

[17]T. K. Roy and A. Ghosh, "Sintering and Grain Growth Kinetics in Undoped and Silica Doped Zinc Oxide Ceramics," *Ceram. Int.*, **40**, 10755–66 (2014).

[18]B. Hatton, V. Kitaev, D. Perovic, G. Ozin, and J. Aizenberg, "Low-Temperature Synthesis of Nanoscale Silica Multilayers - Atomic Layer Deposition in a Test Tube," *J. Mater. Chem.*, **20**, 6009–13 (2010).

[19]Y. Kobayashi, H. Katakami, E. Mine, D. Nagao, M. Konno, and L. M. Liz-Marzan, "Silica Coating of Silver Nanoparticles Using a Modified Stöber Method," *J. Colloid Interface Sci.*, **283**, 392–6 (2005).

[20]J. Zhai, X. Tao, Y. Pu, X.-F. Zeng, and J.-F. Chen, "Core/Shell Structured ZnO/SiO_2 Nanoparticles: Preparation, Characterization and Photocatalytic Property," *Appl. Surf. Sci.*, **257**, 393–7 (2010).

[21]J. T. Luo, X. Y. Zhu, G. Chen, F. Zeng, and F. Pan, "The Electrical, Optical and Magnetic Properties of Si-Doped ZnO Films," *Appl. Surf. Sci.*, **258**, 2177–81 (2012).

[22]J. Rodriguez-Carvajal, "Recent Advances in Magnetic Structure Determination by Neutron Powder Diffraction," *Phys. B*, **192**, 55–69 (1993).

[23]D. J. Larson, T. J. Prosa, R. M. Ulfig, B. P. Geiser, and T. F. Kelly, *Local Electrode Atom Probe Tomography*. Springer, Berlin, Germany, 2013.

[24]M. K. Miller and R. Forbes, *Atom Probe Tomography: The Local Electrode Atom Probe*. Springer, Berlin, Germany, 2014.

[25]M. K. Miller, A. Cerezo, M. G. Hetherington, and G. D. W. Smith, *Atom Probe Field Ion Microscopy*. Clarendon Press, Oxford, 1996.

[26]D. J. Larson, et al., "Field-ion Specimen Preparation Using Focused Ion-Beam Milling," *Ultramicroscopy*, **79**, 287–93 (1999).

[27]M. K. Miller and K. F. Russel, "Atom Probe Specimen Preparation with a Dual Beam SEM/FIB Miller," *Ultramicroscopy*, **107**, 761–6 (2007).

[28]A. J. Melmed, M. Martinka, S. M. Girvin, T. Sakurai, and Y. Kuk, "Analysis of High Resistivity Semiconductor Specimens in an Energy-Compensated Time-of-Flight Atom Probe," *Appl. Phys. Lett.*, **39**, 416–7 (1981).

[29]R. D. Shannon, "Revised Effective Ionic Radii and Systematic Studies of Interatomic Distances in Halides and Chalcogenides," *Acta Cryst. A*, **32**, 751–67 (1976).

[30]L. Brus, "Electronic Wave Functions in Semiconductor Clusters: Experiment and Theory," *J. Phys. Chem.*, **90**, 2555–60 (1986).

[31]S. Ma, H. Liang, X. Wang, J. Zhou, L. Li, and C. Q. Sun, "Controlling the Band Gap of ZnO by Programmable Annealing," *J. Phys. Chem. C*, **115**, 20487–90 (2011).

[32]B. Gault, et al., "Design of a Femtosecond Laser Assisted Tomographic Atom Probe," *Rev. Sci. Instrum.*, **77**, 043705, 8pp (2006).

[33]F. Vurpillot, B. Gault, B. P. Geiser, and D. J. Larson, "Reconstructing Atom Probe Data: A Review," *Ultramicroscopy*, **132**, 19–30 (2013).

[34]R. Haydock and D. R. Kingham, "Post-Ionization of Field-Evaporated Ions," *Phys. Rev. Lett.*, **44**, 1520–23 (1980). □